International Journal of Multiphase Flow 36 (2010) 858–869

Contents lists available at ScienceDirect

International Journal of Multiphase Flow

journal homepage: www.elsevier.com/locate/ijmulflow

A unified spray model for engine spray simulation using dynamic mesh refinement

Ravi Kolakaluri, Yuanhong Li, Song-Charng Kong *

Department of Mechanical Engineering, Iowa State University, 2025 Black Engineering Building, Ames, IA 50011, USA

ARTICLE INFO

Article history:
Received 17 February 2010
Received in revised form 9 July 2010
Accepted 4 August 2010
Available online 12 August 2010

Keywords:
Engine spray
Dynamic mesh refinement
Spray atomization

ABSTRACT

This study is based on dynamic mesh refinement and uses spray breakup models to simulate engine spray dynamics. It is known that the Lagrangian discrete particle technique for spray modeling is sensitive to gird resolution. An adequate spatial resolution in the spray region is necessary to account for the momentum and energy coupling between the gas and liquid phases. This study uses a dynamic mesh refinement algorithm that is adaptive to spray particles to increase the accuracy of spray modeling. On the other hand, the accurate prediction of the spray structure and drop vaporization requires accurate physical models to simulate fuel injection and spray breakup. The present primary jet breakup model predicts the initial breakup of the liquid jet due to the surface instability to generate droplets. A secondary breakup model is then responsible for further breakup of these droplets. The secondary breakup model considers the growth of the unstable waves that are formed on the droplet surface due to the aerodynamic force. The simulation results are compared with experimental data in gasoline spray structure and liquid penetration length. Validations are also performed by comparing the liquid length of a vaporizing diesel spray and its variations with different parameters including the orifice diameter, injection pressure, and ambient gas temperature and density. The model is also applied to simulate a direct-injection gasoline engine with a realistic geometry. The present spray model with dynamic mesh refinement algorithm is shown to predict the spray structure and liquid penetration accurately with reasonable computational cost.

1. Introduction

Due to the competitiveness in the engine industry and the rising environmental concerns, it is necessary to explore a cost-effective way to evaluate the engine performance using different injection strategies, combustion chamber geometries, and alternate fuels. Nowadays, computational fluid dynamics (CFD) has been extensively used to develop new strategies to optimize the engine design. One of the key issues in simulating a direct-injection engine is the proper prediction of the fuel spray dynamics using advanced physical models and numerical schemes. It is known that the prediction of the fuel spray is sensitive to the grid resolution. An adequate grid resolution is required in order to obtain accurate results, especially in the dense spray region (Beard et al., 2000).

Engine sprays are widely modeled by the Lagrangian-drop and Eulerian-fluid technique. The Lagrangian–Eulerian technique is based on the particle–fluid numerical model by Dukowicz (1980), also known as the stochastic parcel method. Each computational parcel consists of a number of droplets that are assumed to have identical properties. On the other hand, there are other approaches based on the Eulerian–Eulerian formulation (Von Berg et al., 2003; Blokkeel et al., 2003; Beck and Watkins, 2004; Baumgarten, 2006). These models use an Eulerian formulation for the spray close to the injector and a Lagrangian formulation for the remaining dilute spray.

In the Lagrangian–Eulerian approach, the Eulerian mesh for the gas phase needs to be adequate in order to avoid the mesh dependence, but the excessive reduction of the grid size for the Eulerian phase may cause a limitation on the Lagrangian liquid phase description. The Lagrangian liquid phase description is based on the assumption of a large void fraction within a cell. The coarse grid size for the Eulerian phase can result in an incorrect prediction in the gas–droplet momentum exchange. Fast diffusion of momentum will occur using a coarse grid, and the predicted spray penetration will be reduced. On the other hand, a cell volume smaller than the actual area of influence of the droplet will cause the gas velocity to exceed the actual velocity, causing spray to over-penetrate. The grid resolution can also affect the collision algorithm used in the model and further influence the simulation results (Schmidt and Rutland, 2000; Beard et al., 2000). For instance, the O'Rourke collision model only considers the collision of droplets in the same cell (Amsden et al., 1989). As the mesh is refined, fewer potential collision partners are present in each cell. Thus, the outcome of collision can depend on the grid resolution, affecting the resulting drop size and spray structure.

---

* Corresponding author.
E-mail address: kong@iastate.edu (S.-C. Kong).

0301-9322/$ - see front matter © 2010 Elsevier Ltd. All rights reserved.
doi:10.1016/j.ijmultiphaseflow.2010.08.001

To help alleviate the problem with mesh dependence, dynamic mesh refinement adapted to spray is an appropriate option. A fine grid resolution is needed primarily in the spray region, and the dynamic mesh refinement can increase the grid resolution in the spray region. Various adaptive mesh refinement algorithms (AMR) were developed for numerous purposes (Biswas and Strawn, 1998; Jasak and Gosman, 2000), particularly for engine spray simulation (e.g., Nomura et al., 2001; Lippert et al., 2005; Xue and Kong, 2009; Li and Kong, 2009a,b).

The accurate prediction of the spray dynamics also requires the use of advanced spray submodels. The nozzle geometry and the flow characteristics (e.g., cavitation) inside the nozzle strongly affect the initial liquid jet conditions. Studies were performed to model the injection process by considering the detailed nozzle geometry and needle lift (Arcoumanis et al., 1997; Hountalas and Kouremenos, 1998). A nozzle model is also available to predict possible flow regimes for different injector geometries and injection conditions (Sarre et al., 1999). The fuel spray is usually modeled for primary breakup and secondary breakup separately. The initial droplets and ligaments formed from the liquid jet are modeled using the primary breakup model. Various models are available to simulate the primary breakup induced by aerodynamic, cavitation, or turbulence forces (Huh and Gosman, 1991; Arcoumanis et al., 1997; Yi and Reitz, 2003). O'Rourke and Amsden (1987) proposed a secondary breakupmodel based on the analogy between a forced oscillating spring-mass system and the drop deformation. Patterson and Reitz (1998) developed a hybrid Kelvin–Helmholtz/Rayleigh–Taylor (KH/RT) model for diesel spray modeling. Beale and Reitz (1999) also applied this model for gasoline spray simulation.

In this study, the collocated version of KIVA-4 (Torres, 2007) is used as the baseline code for model implementation. The dynamic mesh refinement algorithms (Xue and Kong, 2009) are further improved to achieve second-order accuracy at the interface of refined and unrefined cells by improving the convective fluxing calculations at the interface. Various submodels for spray are also implemented. A nozzle flow model is used to simulate the flow inside the nozzle and predict the initial spray injection conditions. A primary breakup model is implemented to track the growth of disturbances and the generation of primary droplets from the cylindrical liquid core. Two secondary breakup models are implemented based on Kelvin–Helmholtz instabilities and Rayleigh–Taylor instabilities.

These models are implemented along with the dynamic mesh refinement and are validated with experimental data for gasoline and diesel sprays. Note that experimental validations of spray modeling using dynamic mesh refinement have not been performed prior to the present study. It should also be noted that traditionally gasoline sprays and diesel sprays are simulated using different models, and adjustments in model constants are often required in order to match experimental data (Kong et al., 1999; Stiesch, 2004; Baumgarten, 2006). The present study uses the same set of models and model constants to simulate both gasoline and diesel sprays under various conditions. The improved dynamic mesh refinement algorithm along with the improved spray models are applied to simulate the mixture formation in a direct-injection gasoline engine with realistic geometries and operating conditions. The use of dynamic mesh refinement on the realistic geometries will provide efficient modeling for the transient engine spray with reduced computational cost.

2. Model formulation

2.1. Base CFD code

The CFD code used in this study is KIVA-4 (Torres and Trujillo, 2006; Torres, 2007). KIVA-4 solves the three-dimensional compressible Navier–Stokes equations and is capable of using unstructured meshes. The original conservation equations (for mass, momentum, and energy), source terms (for spray and combustion), and numerical schemes can be found in the original literature, and thus they are not described in this paper.

KIVA-4 uses the Lagrangian–Eulerian methodology to simulate engine sprays. The original KIVA-4 (Torres and Trujillo, 2006) used a "staggered" approach, in which the velocity is assigned at the node while the remaining cell properties (density, temperature, and pressure) are assigned at the cell center. The code used in this study is based on the "collocated" approach that assigns all cell properties at the cell center, including the velocity (Torres, 2007). The collocation of velocity at the cell center has the advantage of prescribing velocity boundary conditions on the cell faces rather than at the nodes. However, the representation of pressure and velocity at the cell center can cause unphysical pressure oscillations. Thus, the Rhie–Chow technique (Rhie and Chow, 1983; Tsui and Pan, 2006) is used to mitigate these oscillations in this study. In this technique, the flux term $(\boldsymbol{u}\cdot\boldsymbol{A})_f^B$ is modified by the subtraction of the pressure gradient as described in Eq. (1). Note that the variable and convention used in this paper follow those in KIVA-4 (Torres and Trujillo, 2006).

$$(\boldsymbol{u}\cdot\boldsymbol{A})_f^B = (\boldsymbol{u}\cdot\boldsymbol{A})_f^B - \frac{\Delta t}{\frac{1}{2}(\rho_c+\rho_{c_n})}\left[(\Delta p)_f - \frac{1}{2}[(\Delta p)_c + (\Delta p)_{c_n}]\right]\cdot\boldsymbol{A}_f^n \tag{1}$$

where $\boldsymbol{u}$ is the gas velocity $\boldsymbol{A}$ is the area vector. The term $(\boldsymbol{u}\cdot\boldsymbol{A})_f^B$ is used for computing the Lagrangian volume, which is required in the pressure solution. This term is also used in the fluxing algorithm. $(\Delta p)_f$ is the pressure gradient computed at the face, and $(\Delta p)_c$ and $(\Delta p)_{c_n}$ are the pressure gradients computed at the cell centers for the two cells adjacent to face f.

2.2. Dynamic mesh refinement algorithm

The schematic of mesh refinement is shown in Fig. 1. The basic conservation equations for the development of dynamic mesh refinement can be found in Xue and Kong (2009). The implementation of dynamic mesh refinement requires modifications in numerical schemes for the calculation of diffusive and convective fluxes and dynamic timestep adjustment. This study differs from the previous work (Xue and Kong, 2009) in improved algorithms for mesh refinement and enhanced numerical schemes to obtain the second-order accuracy for flux calculation. In the previous mesh refinement approach, the property (i.e., pressure, temperature, etc.) within a parent cell is assumed constant, leading to a first-order approximation for the property of the child cells. In the current approach, a least-squares method is constructed to calculate the cell-centered property of the child cells. In addition, the improved flux calculation at the AMR interface also makes the solver more stable. The changes made in the flux calculation compared to the previous work are discussed below.

The diffusion flux terms with the form $\int_s \nabla Q * d\boldsymbol{A}$ in the conservation equations are the area integrals over surfaces of cells, which

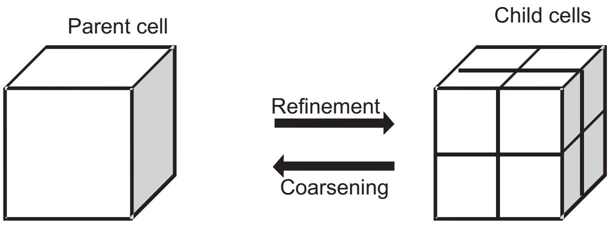

Fig. 1. Schematic of the refinement and coarsening of cells.

can be calculated as the sum over the cell faces using a quadrature rule.

$$\int_s \nabla Q * d\boldsymbol{A} \approx \sum_f (\nabla Q)_f * \boldsymbol{A}_f \tag{2}$$

$$(\nabla Q)_f * \boldsymbol{A}_f = a_c(Q_c - Q_{cn}) + a_{12}(Q_1 - Q_2) + a_{34}(Q_3 - Q_4) \tag{3}$$

Q is any thermodynamic quantity, subscript f represents the cell face, Q_c, Q_{cn} are the cell-centered values of the cells connected to face. Q_1, Q_2, Q_3, and Q_4 are the edge-centered values of the four edges bounding face f, as shown in Fig. 2. These quantities are obtained by averaging the cell-centered values of the cells connected to the edge. The geometric coefficients a_c, a_{12} and a_{34} in Eq. (3) are computed by solving the equations

$$a_c(x_c - x_{cn}) + a_{12}(x_1 - x_2) + a_{34}(x_3 - x_4) = \boldsymbol{A}_f \tag{4}$$

where x_c and x_{cn} are the centers of the cells connected to face f and x_1, x_2, x_3, and x_4 are the centers of the four edges bounding face f. $\boldsymbol{A}_f$ is the face area vector of face f. If face f is an interface between four child cells and one parent cell, the fluxes at the interface will be computed as

$$(\nabla Q * \boldsymbol{A})_{pf} \approx -\sum (\nabla Q * \boldsymbol{A})_{cf} \tag{5}$$

where pf is the parent face, c is the child cell faces, and cf is the child face, as shown in Fig. 3.

The viscous stress tensor $\int_s \sigma * dA$ in the momentum equations is approximated in the same way as in Eq. (2).

$$\int_s \sigma * dA \approx \sum_f \sigma_f * \boldsymbol{A}_f \tag{6}$$

If face f is an interface between the parent cell and four child cells, the term in the left-hand side of Eq. (6) is approximated as

$$(\sigma * \boldsymbol{A})_{pf} \approx -\sum_c (\sigma * \boldsymbol{A})_{cf} \tag{7}$$

The term $(\boldsymbol{u} * \boldsymbol{A})_f^L$ is used to calculate the Lagrangian cell volume V^L that appears in the pressure iteration and is approximated as

$$(\boldsymbol{u} * \boldsymbol{A})_{pf}^L \approx -\sum_c (\boldsymbol{u} * \boldsymbol{A})_{cf}^L \tag{8}$$

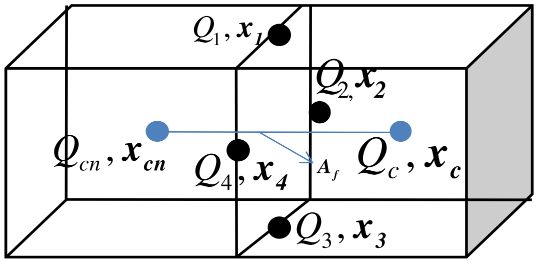

Fig. 2. Geometric arrangement of points to define the gradient of cell-centered quantity Q on cell face f.

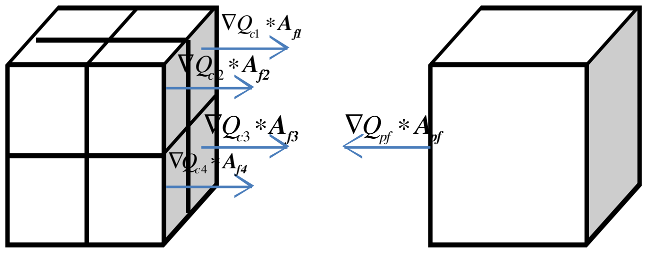

Fig. 3. Gradient calculation at the interface f of the child cells and parent cell.

When the mesh is moved with the fluid in the Lagrangian phase, the mesh is rezoned to the new location, leading to the convective transport of the flow fields due to the relative movement of the mesh. The total computational timestep is explicitly sub-cycled. The number of the sub-cycles is equal to $\Delta t/\Delta t_c$, where Δt is the main computational timestep and Δt_c is the convective timestep that satisfies the Courant condition.

At each sub-cycle the face volume change δV_f associated with cell face f is calculated by considering the total face volume change from the Lagrangian position to the final position after rezoning. The following formula is used to calculate the volume change,

$$\delta V_{f_c} = \delta V_{fc}^{n+1,n} \frac{\Delta t_c}{\Delta t} - \Delta t_c (\boldsymbol{u} \cdot \boldsymbol{A})_{cf}^L \tag{9}$$

where $\delta V_{fc}^{n+1,n}$ is the total volume change of the face f of the cell from the location at time n to the final location at time $n + 1$. If δV_f is positive, the face movement leads to the cell volume expansion or, if it is negative, to the cell volume compression.

The convective fluxes in the conservation equations are explicitly sub-cycled and the flux through a normal face into a cell is calculated as

$$(\rho Q V)_c^s = (\rho Q V)_c^{s-1} + (\rho Q)_f^{s-1} * \delta V_f \tag{10}$$

where ρ is the density, V is the volume, c is the cell considered, s is the current sub-cycle, $s - 1$ represents the previous sub-cycle, and Q represents the cell-centered quantity. $(\rho Q)_f$ is determined by using a quasi-second-order upwind (QSOU) scheme at each sub-cycle. If the face is a coarse–fine interface, Eq. (10) will change to

$$(\rho Q V)_p^s = (\rho Q V)_p^{s-1} - \sum_c (\rho Q)_{fc}^{s-1} * \delta V_{fc} \tag{11}$$

where p represents the parent cell and c is the number of child cell at the coarse–fine interface face.

The convective time step in the algorithm is also modified to account for mesh movement and the cell size change resulting from the refinement/coarsening as

$$\Delta t_c^n \leqslant C_c \Delta t_c^{n-1} \min_f \frac{V}{|\delta V_f|} \tag{12}$$

where δV_f is the face volume change, Δt_c^{n-1} is the previous time step, V is the cell volume, and C_c is a constant equal to 0.2. The above equation is calculated at the beginning of each computational cycle. The geometrical volume of the newly refined cell is approximately one-eighth of the parent cell and the face area is approximately one-fourth of the parent cell. For the newly refined cells, the convective time step is a half of the time step for the parent cell.

To test the accuracy of the current approximation approach that involves the AMR interface, a linear polynomial of a cell-centered quantity is assumed within each child cell that has an AMR interface. This polynomial is then used to calculate a theoretical flux across the interface of the child cell with second-order accuracy. In the mean time, a flux using the present approximation is also calculated. If the ratio of the two fluxes is equal to unity, it is believed that the current approximation is second-order accurate because the theoretical flux is calculated in second-order accuracy. A numerical test was conducted in this study to validate the accuracy of the present approximation approach. In order to account for all the AMR interfaces, the average of the ratio of the two fluxes over all the child cell interfaces was evaluated. In this test, the in-cylinder flow and fuel injection were simulated in a cylindrical chamber with a moving piston, and the turbulent kinetic energy was chosen as the cell-centered quantity for flux calculation. The simulation was from 180 ATDC to 360 ATDC. Fig. 4 shows the

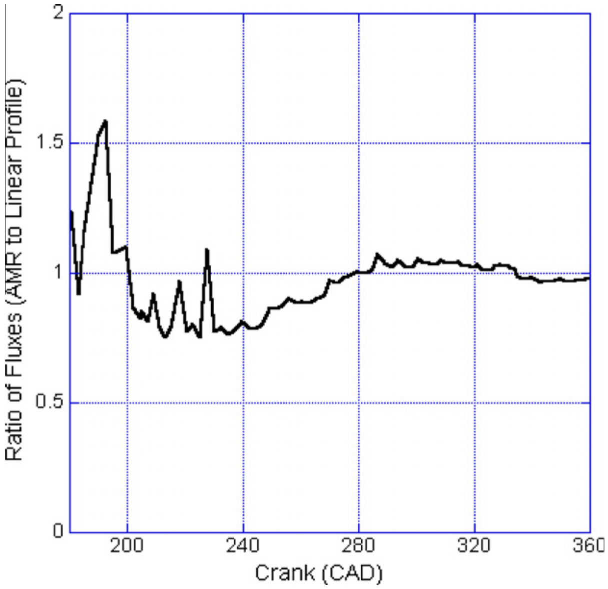

Fig. 4. The averaged ratio of the AMR flux to the theoretical flux based on a linear profile at the AMR interface for the turbulent kinetic energy in an engine chamber with a flat piston.

history of the ratio of the two fluxes. It can be seen that this ratio is close to unity most of the time, indicating that the present approach can reach second-order accuracy.

In this study, the refinement and coarsening criterion is the sum of the fuel drop and fuel vapor mass in each cell. A threshold value of 1×10^{-6} g is chosen after a series of simulation studies (Xue and Kong, 2009). This value is chosen based on the consideration of the mesh density requirement and computational cost. The present criterion works satisfactorily in engine spray simulation, and the threshold value remains unchanged during simulation. Notice that other criteria such as velocity gradients can also be used to resolve the fuel spray if desired. It is also worth noting that the AMR technique itself is not intended to reduce the mesh dependence. Rather, the purpose of AMR is to provide adequate grid resolution for spray modeling, e.g., typically 1–2 mm cell size (Abraham, 1997; Lippert et al., 2005). When fuel spray is no longer present in the domain, the original grid can be restored to avoid using a uniformly fine mesh for the entire simulation. As a result, the computer time can be reduced.

2.3. Nozzle flow model

A nozzle flow model provides initial spray conditions for the subsequent breakup simulation. In direct-injection gasoline and diesel engines, the injector nozzle geometry affects the fuel atomization and also influences engine combustion and emissions. The nozzle flow model (Sarre et al., 1999) is implemented in this study. The conditions inside the nozzle can be estimated from the nozzle geometry (r_{noz}/d_{noz}, radius to diameter ratio of nozzle and l_{noz}/d_{noz}, length to diameter ratio of nozzle), injection pressure, and ambient pressure (p_2). The model output includes discharge coefficient (C_d), effective velocity (U_{eff}), average turbulent kinetic energy, spray angle, and initial drop size. The nozzle upstream pressure (p_1) can be initially estimated and will be modified depending on the type of flow inside the nozzle.

The pressure at vena contracta is then computed and compared with the saturated vapor pressure (p_{vapor}) to decide whether cavitation occurs in the nozzle. The values of p_1, C_d and $\boldsymbol{U}_{eff}$ can be determined by the following relations.

$$p_1 = p_{vapor} + \frac{\rho}{2} * \boldsymbol{U}_{vena}^2 \tag{13}$$

$$C_d = C_c * \sqrt{\frac{p_1 - p_{vapor}}{p_1 - p_2}} \tag{14}$$

$$\boldsymbol{U}_{eff} = \boldsymbol{U}_{vena} - \frac{p_2 - p_{vapor}}{\rho_l * \boldsymbol{U}_{mean}} \tag{15}$$

The nozzle contraction coefficient (C_c) and velocity at the vena contracta ($\boldsymbol{U}_{vena}$) are determined by the nozzle geometry. The mean flow velocity ($\boldsymbol{U}_{mean}$) is calculated based on the flow rate and nominal nozzle area (Sarre et al., 1999).

2.4. Primary breakup model

The breakup of the liquid jet at the nozzle exit is modeled using a primary breakup model (Yi and Reitz, 2003) by which the secondary droplets are created. The model tracks the growth of the disturbance on the jet surface leading to the generation of droplets. The surface structure obtained from the model is decomposed into a combination of waves using a fast Fourier transform. Initially, a disturbance, which is a combination of waves due to the nozzle flow, is applied to the undistributed jet leaving the nozzle exit. The initial disturbance is represented as

$$R(0,x) = R_0 + \frac{1}{n}\sum_{i=1}^{n} \eta_i \sin(\omega_i x + \varphi_i) \tag{16}$$

$$\eta_i = \eta_0 * f(\lambda_i) \tag{17}$$

where R is the initial jet radius at axial position x. R_0 is the undisturbed jet radius, ϕ_i is the phase of the i_{th} wave, and n is the number of waves. η_i is the initial amplitude, and η_0 is the amplitude of the most probable wave with a wavelength λ_0. $f(\lambda_i)$ is the value of the normalized Gaussian distribution for the i_{th} wave, where $f(\lambda_0) = 1$. The tracking of the disturbance growth is accomplished using a 1-D model approach,

$$\frac{\partial R^2}{\partial t} = -\frac{\partial R^2 u}{\partial x} \tag{18}$$

$$\frac{\partial R^2 u}{\partial t} + \frac{\partial R^2 u^2}{\partial x} = -\frac{R^2}{\rho_l}\left(\frac{\partial p_l}{\partial x} + \frac{\partial p_g}{\partial x}\right) + 2\nu_l \frac{\partial}{\partial x}\left(R^2 \frac{\partial u}{\partial x}\right) \tag{19}$$

where t is time and x is the axial coordinate with its positive direction pointing in the flow direction of the jet. $R = R(t, x)$ and $u = u(t, x)$ are the velocity and radius of the liquid jet respectively, as a function of time and axial position, and ρ_l and ν_l are the density and viscosity of the liquid, respectively, p_l is the pressure caused by the liquid surface tension, and p_g is the pressure exerted by the gas inertia.

The jet surface structure obtained from the model is divided into a breakup zone and a liquid core. Drops are stripped from the breakup zone after a breakup time is achieved and their number depends on the mass of liquid in the breakup zone. The breakup time and the drop size are obtained by solving Eqs. (18) and (19). To determine the time of breakup, the increase in the total jet surface area due to the growth of the unstable wave is tracked and compared to the total surface area of the drops that will be formed at the time of the breakup. When these two areas become equal, breakup occurs and primary drops are formed. The reference wavelength and amplitude of the initial disturbance are chosen as $\lambda_0 = 20\ \mu\text{m}$ and $\eta_0 = 0.01\lambda_0$, respectively (Yi and Reitz, 2003). This wavelength is at the same order as the SMD of a typical high-speed diesel spray. In fact, it is found that the effect of the above chosen values on the prediction of the breakup time and drop size is negligible.

2.5. Secondary breakup model

The further breakup of already existing droplets into smaller droplets takes place subsequently and is simulated by a secondary breakup model. The breakup of droplets takes place due to the aerodynamic forces that are induced by the relative velocity between the droplet and the surrounding gas. In the model, unstable waves are allowed to grow on the droplet surface due to these aerodynamic forces leading to further atomization. The model used for the secondary breakup is the hybrid KH/RT model (Patterson and Reitz, 1998). The KH model is based on a first-order linear analysis of the KH instabilities growing on the surface of a cylindrical jet (Reitz, 1987). This model was previously applied to drop atomization modeling by monitoring the surface wave growth rate Ω and wavelength Λ (Reitz, 1987). Child droplets are formed when breakup criteria are met.

The radius of the child drop (r') is proportional to the wavelength Λ of the most unstable surface wave,

$$r' = B_0 * \Lambda \tag{20}$$

The constant B_0 used in Eq. (20) determines the size of the droplet formed from a parent drop and is 0.61 for diesel sprays. This constant describes the size of droplet compared to the wavelength of the Kelvin–Helmholtz wave. The mass of the parent drop is reduced based on the mass conservation. The reduction of the radius of the parent drop depends on the initial size of the parent drop (r) and the breakup time τ.

$$\frac{dr}{dt} = -\frac{r - r'}{\tau} \tag{21}$$

$$\tau = 3.788 * B_1 \frac{r}{\Lambda * \Omega} \tag{22}$$

The breakup time constant B_1 used in Eq. (22) determines how quickly the parent drop breaks up to form child droplets. This constant has been given a variety of values between 10 and 60. However, for the simulation of direct injection spray, a value of 40 is used in this study as recommended by Kong et al. (1999).

The RT model is based on the theory of Taylor (1963) on wave stability. The interface between the gas and liquid is unstable when the acceleration is directed into the gas and the unstable disturbances can grow with acceleration. Due to the deceleration of the drop due to the drag forces, unstable waves can grow on the backside of the drop and the disintegration of the drop will take place when a critical limit is achieved. The acceleration of the interface of the gas and the drop due to the drag force can be found as

$$a = \frac{3}{8} C_D \frac{\rho_g u_{rel}^2}{\rho_l r} \tag{23}$$

where C_D is the drag coefficient of the drop, u_{rel} is the relative velocity between the gas and liquid drop, and ρ_g and ρ_l are the gas density and liquid drop density, respectively. The linear stability analysis is used to find the growth rate Ω and the corresponding wavelength Λ of the fastest growing wave. The new drop radius and the breakup timescale can be determined from

$$r' = \frac{C_3 * \Lambda}{2} \tag{24}$$

$$\tau = \frac{1}{\Omega} \tag{25}$$

where r' the radius of the new drop, C_3 is a constant that changes the radius of the new droplet and τ is the breakup time. The model tracks the time of the individual drop since last breakup. When breakup time is reached, new drops are formed with radius r' and the breakup time is reset to zero.

In the secondary breakup region, both the KH and RT models are allowed to grow the unstable waves simultaneously. The disintegration of a drop will occur when one of the KH or RT models predicts breakup to occur.

3. Results and discussions

The present model with dynamic mesh refinement is applied to simulate both gasoline and diesel sprays. The computational domain is a constant-volume cylindrical chamber with 100 mm in diameter and 100 mm in length, as shown in Fig. 5. The average mesh size is 5 mm prior to refinement. Note that the base mesh is relatively coarse and the mesh will be refined in the spray region by the present AMR algorithm. The experimental data used for gasoline spray validation include spray images and penetration data of a 10-hole gasoline injector that is used in direct-injection gasoline engines. The present model is also validated using the high-pressure diesel spray data obtained from high-pressure, high-temperature conditions in a constant-volume chamber (Siebers, 1998). The model is also used to simulate gasoline spray in realistic engine geometry.

3.1. Gasoline spray modeling

The test conditions for gasoline spray experiments are listed in Table 1 and the nozzle geometrical parameters are given in Table 2. The predicted spray drop distributions are shown in Fig. 6 for different simulation conditions. It can be seen that the predicted spray penetration is shorter using a coarse mesh. The shorter penetration is due to the fast diffusion of momentum on the coarse mesh. Additionally, to some extent the collision model is mesh dependent because only the particles in a particular cell participate in collision. However, with the use of AMR based on the coarse mesh, the fast diffusion of momentum can be avoided by using a fine mesh in the spray region, which is similar to the use of a fine

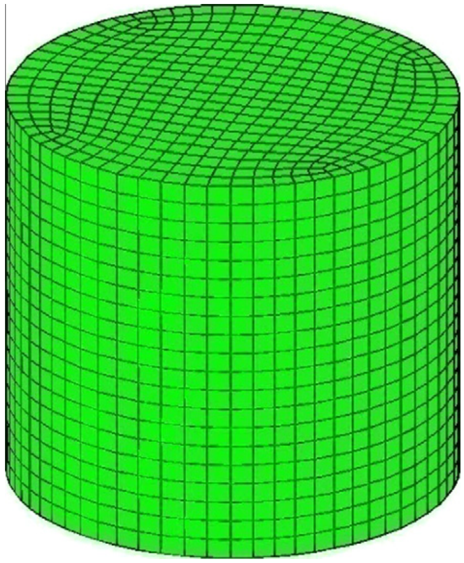

Fig. 5. Computational mesh of the cylindrical chamber for model validation.

Table 1
Conditions for the gasoline sprays.

Fuel	Gasoline
Ambient gas pressure	1–5 bar
Ambient gas density	1.15–5.8 kg/m^3
Ambient gas temperature	300 K
Orifice diameter	130 µm
Number of orifices	10
Fuel temperature	300 K
Injection pressure	60–120 bar

Table 2
Nozzle geometry and injection parameters for gasoline spray.

Injection type	Pulsed (velocity profile)
r/*d*	0.03
l/*d*	3.3
Aconst	4.0
Cone angle	9°

mesh. Thus, the predicted spray structure and droplet distribution using AMR on the coarse mesh are similar to those predicted using the fine mesh. These results indicate that the present AMR algorithm can be used to obtain the same level of accuracy in spray modeling without the need to use a very fine mesh (e.g., Fig. 6c). As a result, a speed-up in computer time can be achieved. A study on the speed-up due to use of AMR has been reported in detail in a previous publication (Xue and Kong, 2009).

The numerical results are compared with experimental data on spray structure and liquid penetration. Experimental data on both the gasoline spray (Yi, 2009) and diesel sprays (Siebers, 1998) are used for model validation. The predicted liquid penetration length is defined as the location from the nozzle within which 95% of the total liquid mass is contained. This definition is commonly used for comparing numerical and experimental penetrations (Yi and Reitz, 2003).

Fig. 7 shows the comparison of the experimental images (Yi, 2009) and the predicted drop distributions for injection pressure 100 bar and back pressure 1 bar at 0.7 ms after injection. The spray penetrations predicted by the model are in good agreement with the experimental data. Qualitatively speaking, the predicted droplet distribution is also satisfactory. Fig. 8 shows the comparison at 1.6 ms after injection with the same conditions. The spray structure and the droplet distribution are well predicted using the present model.

The effects of back pressure on the penetration of gasoline sprays are also modeled and the results are compared with the experimental data, as shown in Fig. 9. The level of back pressure will affect the momentum of the spray. With an increase in back pressure, the drag force experienced by spray particles increases, which will enhance the early breakup of droplets but reduce the spray tip penetration. The injection pressure is maintained constant and the back pressure is varied in this study. The experimental penetration data of the gasoline spray are obtained by measuring manually from images. Some of the results do not follow a particular trend (linear or exponential). The predicted penetration decreases as the back pressure increases, as also observed in the experiments. The simulation over-predicts the penetration in the 1 bar case as compared to the experimental data. This disagreement can be attributed to the uncertainties in the manual measurements of the penetration and the empirical constants used in the spray models. However, it should be noted that same model

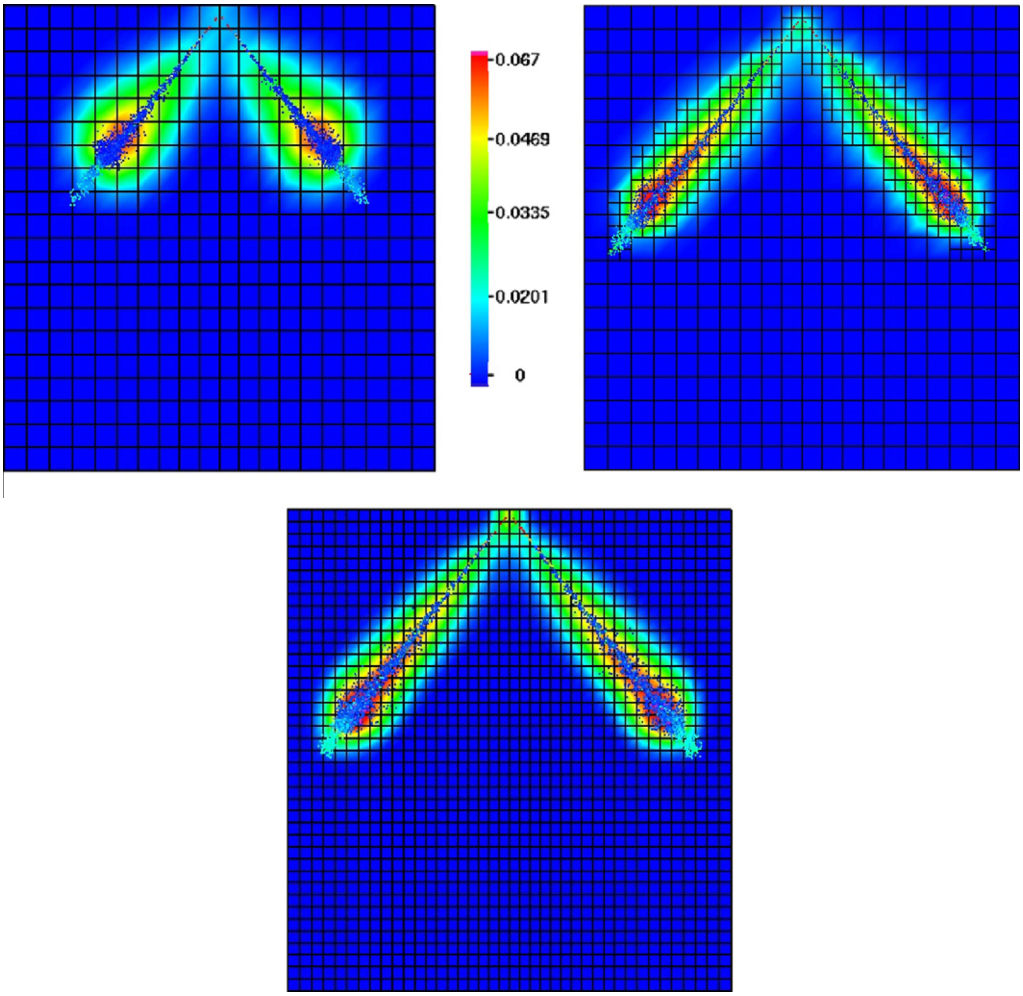

Fig. 6. Predicted drop and vapor distributions of the gasoline spray at 1.6 ms after injection (injection pressure 100 bar, back pressure 1 bar, gas density 1.16 kg/m^3, gas temperature 300 K and orifice diameter 130 μm).

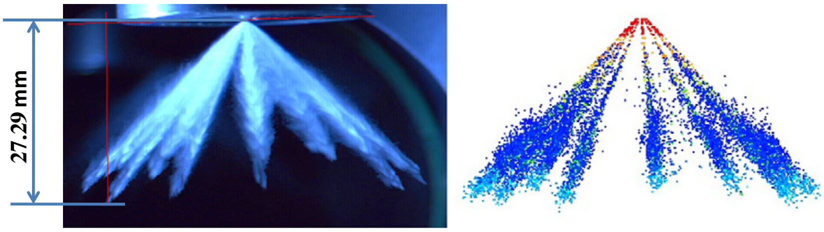

Fig. 7. Experimental image and predicted spray structure of the gasoline spray at 0.7 ms after injection. Injection pressure, back pressure, gas density, gas temperature and orifice diameter are 100 bar, 1 bar, 1.16 kg/m^3, 300 K and 130 µm, respectively.

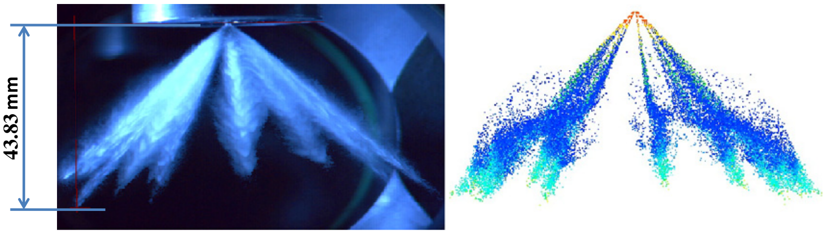

Fig. 8. Experimental image and predicted spray structure of the gasoline spray at 1.6 ms after injection. Injection pressure, back pressure, gas density, gas temperature and orifice diameter are 100 bar, 1 bar, 1.16 kg/m^3, 300 K and 30 µm, respectively.

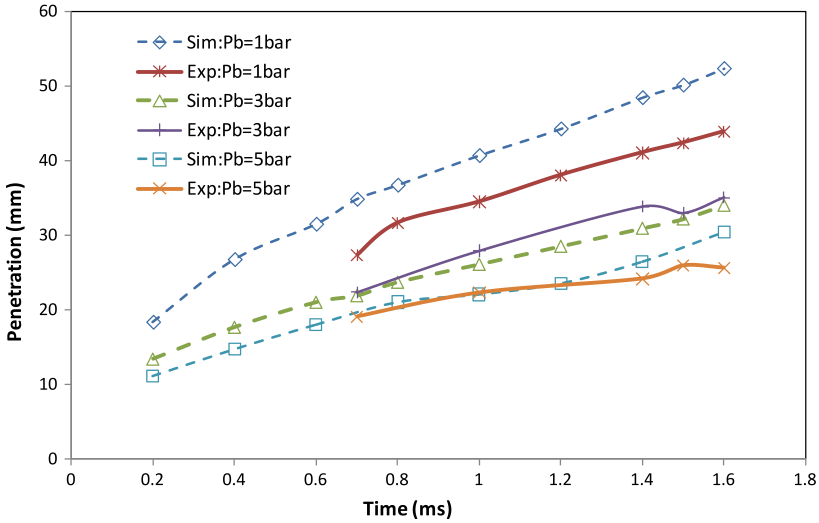

Fig. 9. Effects of back pressure on the liquid penetration history. Injection pressure, gas density, gas temperature and orifice diameter are 100 bar, 1.16–5.78 kg/m^3, 300 K and 130 µm, respectively.

constants are used for both gasoline and diesel spray modeling. The agreement in most of the cases studied is reasonably well. The uncertainties in experimental data can further be observed in Fig. 10, where the measured penetrations of both injection pressure of 100 and 120 bar almost overlap on each other. In Fig. 10, the predicted spray penetrations using different injection pressures are compared with experimental data. Speaking overall, the simulation results agree with experimental data in which liquid penetrations increase with increased injection pressure. The model is able to predict the trend as well as the actual liquid penetration length. Overall speaking, the present primary atomization model and the hybrid KH/RT model with dynamic mesh refinement are able to predict the spray penetration and spray structure correctly.

3.2. Diesel spray modeling

The model is further validated by comparing the simulation results with the experimental diesel spray data under various conditions (Siebers, 1998). The liquid length is the maximum axial penetration of the liquid phase fuel in a vaporizing diesel spray. The parameters that are varied include the orifice diameter, fuel temperature, and ambient gas temperature and density. The conditions are given in Table 3.

The effect of the ambient gas density on the liquid length is shown in Fig. 11. Note that the liquid penetration reached a steady-state length due to the continuous vaporization of leading drops. The simulation results show that the liquid length decreases with increased ambient gas density since it is more difficult for drops to penetrate in a high-density environment. The model results agree well with the experimental data for the 850 K and 1000 K cases. The model over-predicts penetration for the 1300 K case, particularly at the higher density region. This deviation can be attributed to the inability of the model at the higher density and temperature conditions in which there is less diffusive of momentum. Such outcomes may provide guidelines for future model improvement. The results are re-plotted in Fig. 12 such that

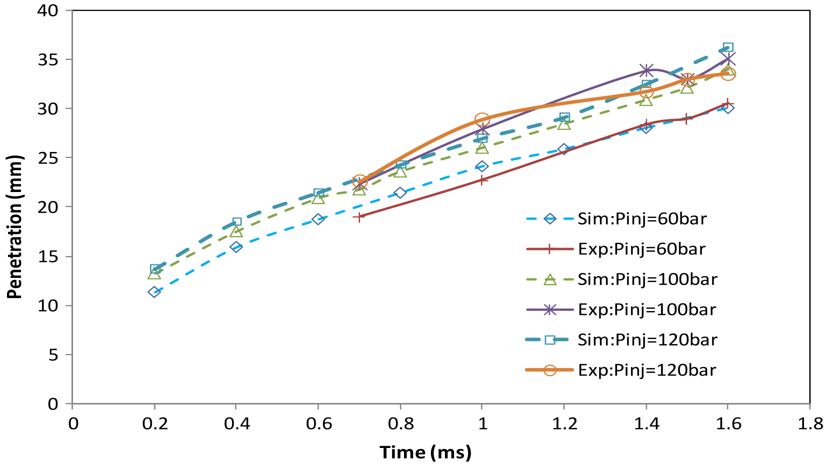

Fig. 10. Effects of injection pressure on the liquid penetration history. Back pressure, gas temperature and orifice diameter are 3 bar, 3.47 kg/m^3, 300 K and 130 μm, respectively.

Table 3
Conditions for the diesel spray.

Fuel	HMN (C16H34)
Ambient gas density	3.3–60 kg/m^3
Ambient gas temperature	700–1300 K
Fuel temperature	375–440 K
Orifice diameter	100–500 μm
Orifice pressure drop	130–150 MPa
Number of orifices	1

the effect of ambient temperature on the liquid length can be readily identified. Simulation results follow the general trend that the liquid length decreases with increased gas temperature due to high vaporization rate of liquid fuel in high-temperature environments. The model also slightly over-predicts the liquid length at the high temperature condition, and this might be due to the same reason given above.

Fig. 13 shows the variation of the liquid length with the orifice diameter. The liquid length increases linearly with an increase in the orifice diameter. This is because a small nozzle hole produces small drops that atomize and vaporize more easily. Additionally, the large drops resulting from the large orifice have higher momentum to penetrate farther into the combustion chamber. In the actual diesel engine application, a smaller orifice is generally preferred due to its capability to produce better fuel–air mixing to reduce soot emissions (Pickett and Siebers, 2004).

The effect of the fuel temperature on the liquid length is also modeled and the results are compared with the experimental data as shown in Fig. 14. The decrease in the liquid length with increased fuel temperature is predicted correctly using the present model. A high fuel temperature enhances vaporization and thus reduces the liquid penetration. The effects may seem small, however, this is due to the small temperature range studied, i.e., 375–440 K. The effect of fuel temperature on the liquid length is more pronounced at the low ambient gas temperature condition. For instance, the decrease in the liquid length is approximately 10% for a 65 K increase in the ambient temperature for ambient density of 14.8 kg/m^3 and temperature of 995 K.

It should be noted that traditionally the gasoline spray and diesel spray are modeled using different breakup models (Kong et al., 1999). The model by O'Rourke and Amsden (1987) has been widely used for gasoline spray breakup simulation while the KH–RT model (Patterson and Reitz, 1998) is used for diesel spray modeling. Despite that the KH–RT model was used for gasoline hollow-cone spray modeling by Beale and Reitz (1999), the primary jet breakup

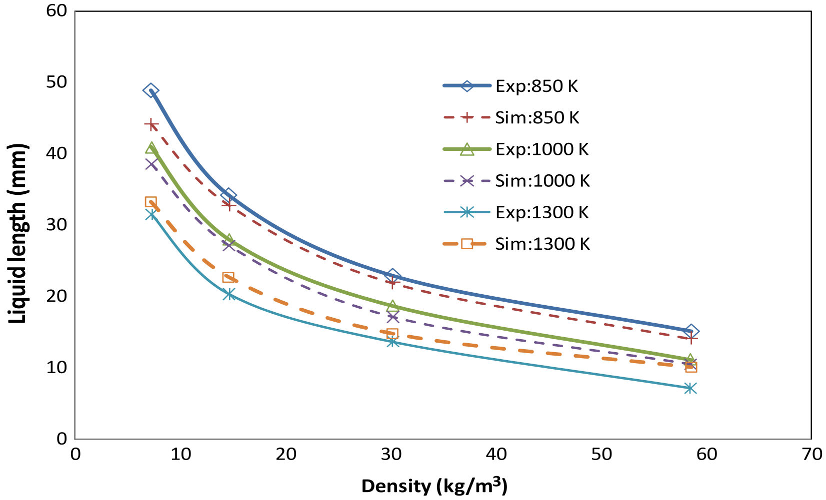

Fig. 11. Liquid length as a function of the ambient gas density. The injection pressure, fuel temperature and orifice diameter are 136 MPa, 438 K and 246 μm.

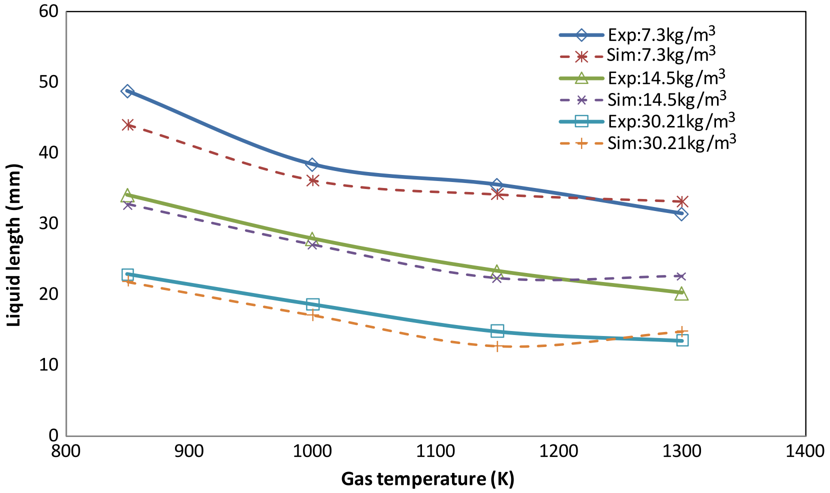

Fig. 12. Liquid length as a function of ambient gas temperature. The injection pressure, fuel temperature and orifice diameter are 136 MPa, 438 K and 246 µm, respectively.

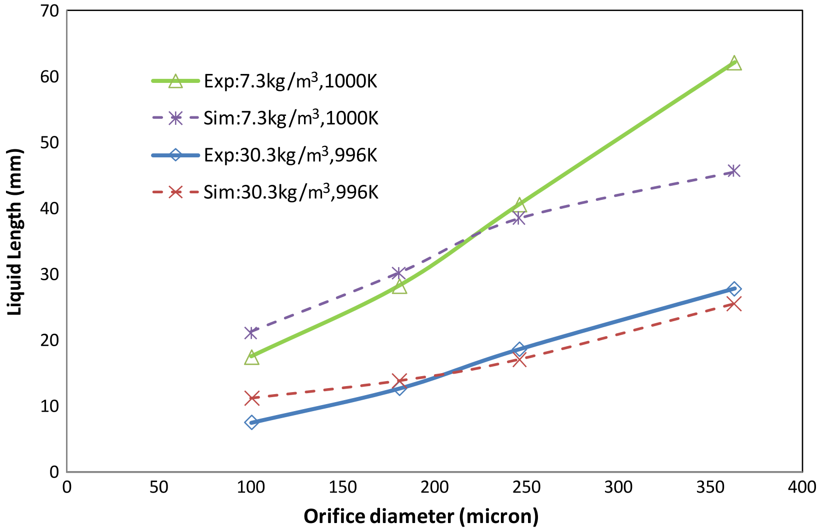

Fig. 13. Liquid length as a function of orifice diameter. The injection pressure and fuel temperature are 135 MPa, and 438 µm, respectively.

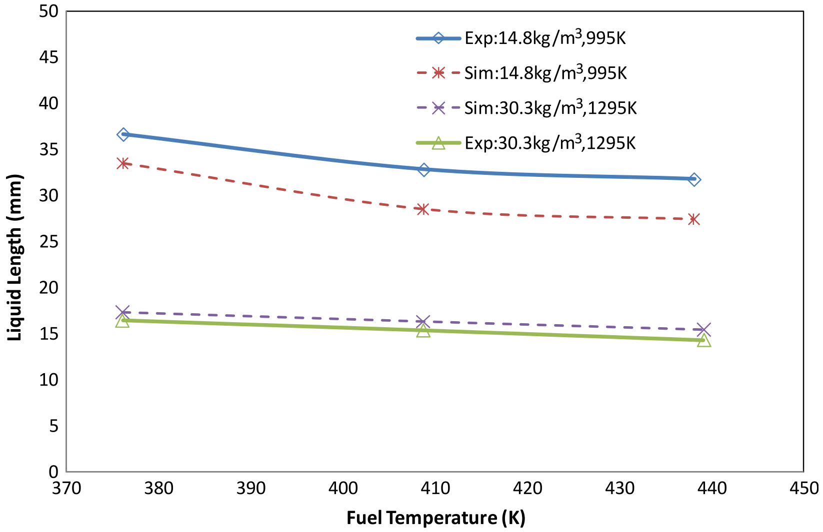

Fig. 14. Liquid length as a function of fuel temperature. The injection pressure and orifice diameter are 135 MPa, and 246 µm, respectively.

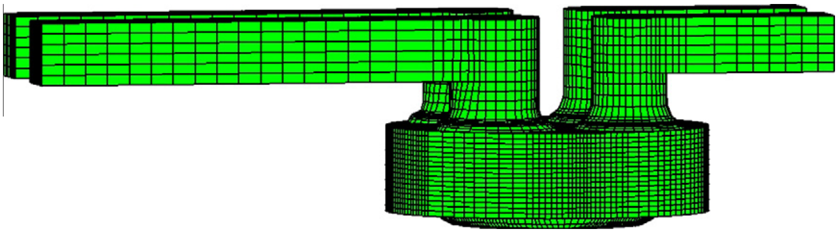

Fig. 15. Computational mesh of the present gasoline engine.

Table 4
Conditions for the present direct-injection gasoline engine.

Bore and stroke (cm)	10.375 and 10.755
Engine speed (rpm)	1000
Fuel	Gasoline
Initial gas temperature and pressure	300 K and 1 bar
Orifice diameter and fuel temperature	100 μm and 300 K
Number of orifices	6
Computation duration	300–720 ATDC
Start of injection	400 ATDC
Injection duration	60 ATDC
Injected fuel mass	0.060 g/s
Averaged injection velocity (cm/s)	13,500
Intake valve (open/closure)	370/608 ATDC
Exhaust valve (open/closure)	106/372 ATDC

was not modeled and thus a prescribed initial drop size distribution was used to initiate the breakup process. The new contribution of the present study is to use an integrated nozzle flow model and primary and secondary breakup models to simulate both gasoline and diesel sprays. Model results are in good agreement with experimental data over a wide range of conditions without adjustments in model constants. Additionally, the present dynamic mesh refinement also allows the user to use a coarse baseline mesh for efficient computation.

3.3. Direct-injection gasoline engine modeling

The present model is also applied to simulate the in-cylinder spray process in a direct-injection gasoline engine. The computational mesh is shown in Fig. 15. The bore is 103.75 mm and the stroke is 107.55 mm. A baseline coarse mesh on this geometry has approximately 80,000 cells and a further refined mesh would be computationally expensive. Thus, it is appropriate to use a coarse mesh with dynamic mesh refinement that can provide proper grid resolution in the spray region to avoid the use of a very

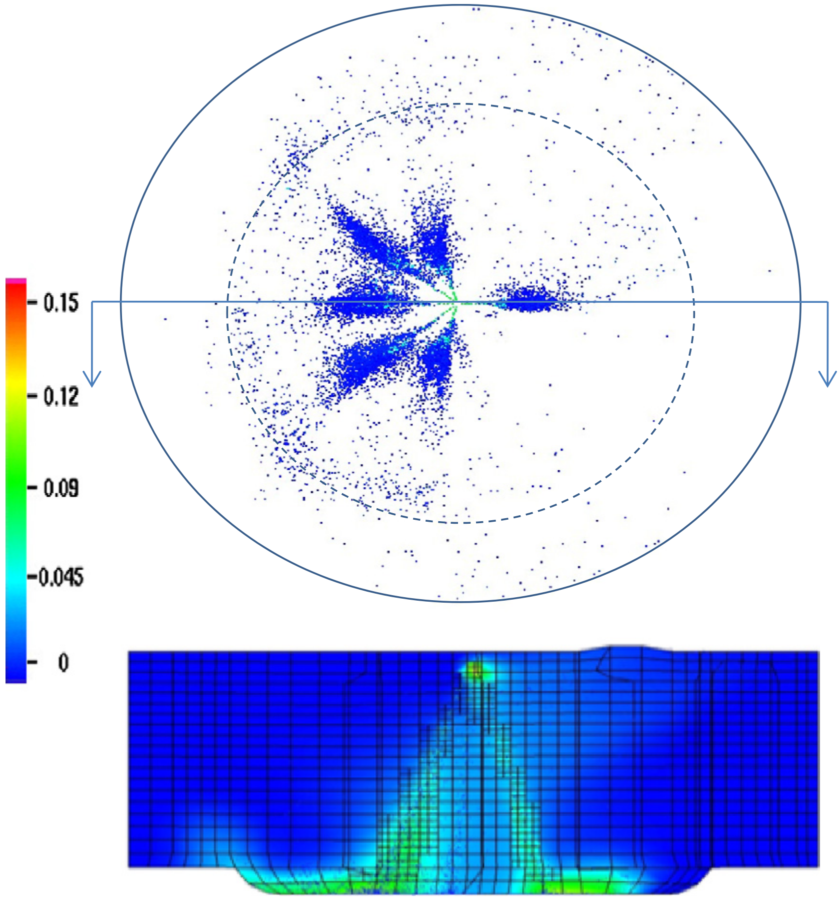

Fig. 16. Predicted fuel drop distributions and fuel vapor mass fraction on two views at 420 ATDC. The injection timing was 400 ATDC. The scale shown is the fuel mass fraction.

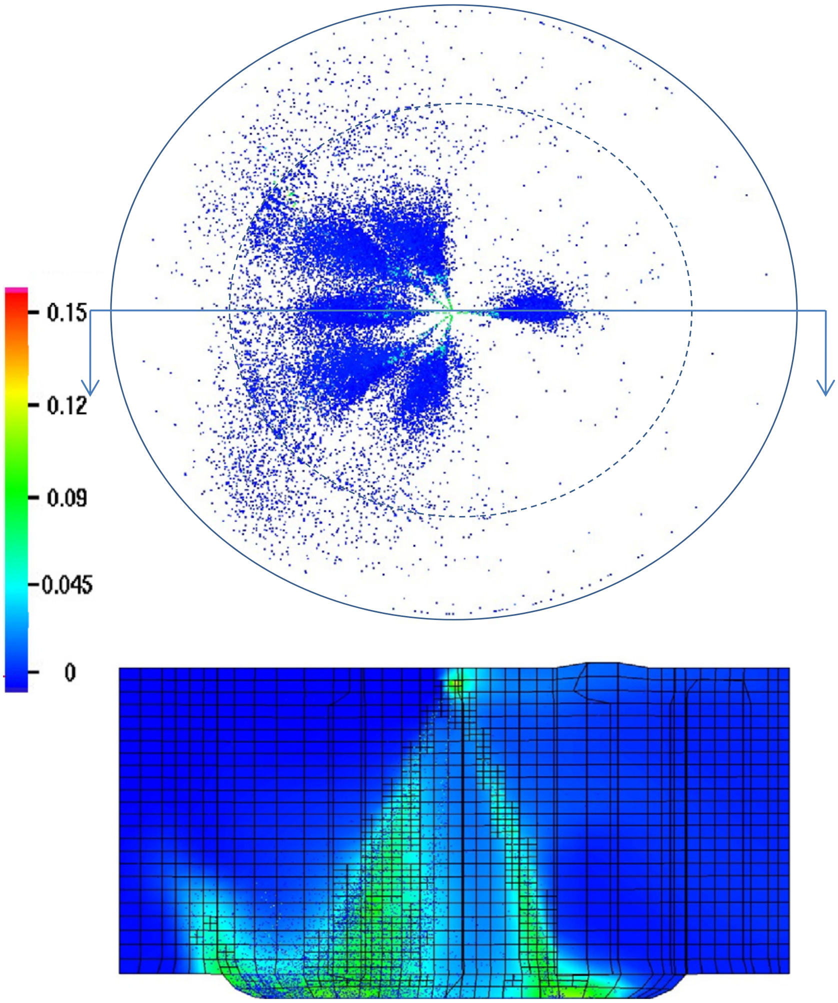

Fig. 17. Predicted fuel drop distributions and fuel vapor mass fraction on two views at 440 ATDC. The injection timing was 400 ATDC. The scale shown is the fuel mass fraction.

fine mesh. Note that this study is focused on the application of dynamic mesh refinement and spray models. Benchmark studies on computer time using different mesh densities are not performed. More details on the comparison of computer times using different meshes can be found in Xue and Kong (2009).

The engine operating conditions are given in Table 4. Figs. 16 and 17 show the liquid drop distribution on two different views at two different times. Note that this particular injector was designed to have asymmetric nozzle arrangement. Five nozzles point towards one side, and the other nozzle point towards the other side. Thus, the spray patterns shown in the figures are not symmetric. This nozzle arrangement was designed to achieve desirable mixture distributions in the cylinder considering the intake flow structure and combustion chamber geometry (Yi, 2009). The mesh and fuel vapor mass fraction on a cut-plane are also shown. The cut-plane is across two fuel jets and through the center of the cylinder. It can be seen that locally fine mesh is generated in the spray region in order to increase the spray modeling accuracy. It is worth noting that the primary concern in a direct-injection engine is the proper mixing of fuel and air within a relatively short timescale during engine operation. The mixture distribution will further affect the combustion and emissions performance of an engine. Despite that in-cylinder experimental data are not available for detailed model validation, this study demonstrates that the present model together with the AMR algorithm can be applied to engine simulation under realistic geometries and conditions with piston motion and moving boundaries.

4. Conclusions

In this study various spray submodels are implemented, including a nozzle flow model, a primary jet breakup model, and a secondary drop breakup. The overall model is validated using experimental data of low-pressure gasoline sprays and high-pressure diesel sprays. Good levels of agreement are obtained in liquid penetration and spray structure under various operating conditions.

The model predicts correctly the liquid penetration history of the present gasoline spray for different injection pressures and ambient pressures. In the diesel spray validation, the model is also able to capture the effects of various parameters on the liquid penetration, including ambient gas temperature and density, injection pressure, fuel temperature, and nozzle diameter. This study demonstrates that the present model with mesh refinement schemes can be successfully applied to engine spray simulation with satisfactory performance.

The application of adaptive mesh refinement in modeling realistic engine geometries is also demonstrated in this study. The present mesh refinement scheme can allow the use of a coarse baseline mesh for better computational efficiency.

Acknowledgement

The authors acknowledge the financial support of Ford Motor Company.

References

Abraham, J., 1997. What Is Adequate Resolution in the Numerical Computation of Transient Jets? SAE Paper 970051.

Arcoumanis, C., Gavaises, M., French, B., 1997. Effect of Fuel Injection Process on the Structure of Diesel Sprays, SAE Paper 970799.

Amsden, A.A., O'Rourke, P.J., Butler, T.D., 1989. KIVA-II: A Computer Program for Chemically Reactive Flow with Sprays, Technical Report, Los Alamos National Laboratory, LA-11560-MS.

Baumgarten, C., 2006. Mixture Formation in Internal Combustion Engines. Springer-Verlag, Berlin, Heidelberg.

Beale, J.C., Reitz, R.D., 1999. Modeling spray atomization with the Kelvin–Helmholtz/Rayleigh–Taylor hybrid model. Atomization Sprays 9, 623–650.

Beard, P., Duclos, J.M., Habchi, C., Bruneaux, G., Mokkadem, K., Baritaud, T., 2000. Extension of Lagrangian–Eulerian Spray Modeling: Application to High Pressure Evaporating Diesel Sprays, SAE Paper 2000-01-1893.

Beck, J.C., Watkins, A.P., 2004. The simulation of fuel sprays using the moments of the drop number size distribution. Int. J. Engine Res. 5, 1–21.

Biswas, R., Strawn, R.C., 1998. Tetrahedral and hexahedral mesh adaptation for CFD problems. J. Appl. Numer. Math. 26, 135–151.

Blokkeel, G., Mura, A., Demoulin, F.X., Borghi, R., 2003. A 3D Eulerian Model to Improve the Primary Breakup of Atomizing Jet, SAE Paper 2003-01-0005.

Dukowicz, J.K., 1980. A particle-fluid numerical-model for liquid sprays. J. Comput. Phys. 35, 229–253.

Hountalas, D.T., Kouremenos, A.D., 1998. Development of a fast and simple simulation model for the fuel injection system of diesel engines. Adv. Eng. Software 29, 13–28.

Huh, K.Y., Gosman, A.D., 1991. A Phenomenological Model of Diesel Spray Atomization. In: Proceedings of International Conference on Multiphase Flow.

Jasak, H., Gosman, A.D., 2000. Automatic resolution control for the finite volume method, part 2: adaptive mesh refinement and coarsening. Numer. Heat Transfer B 38, 257–271.

Kong, S.-C., Senecal, P.K., Reitz, R.D., 1999. Developments in spray modeling in diesel and direct-injection gasoline engines. Oil Gas Sci. Technol. – Rev. IFP 54, 197–204.

Li, Y., Kong, S.-C., 2009a. Mesh refinement algorithms in an unstructured solver for multiphase flow simulation using discrete particles. J. Comput. Phys. 228, 6349–6360.

Li, Y., Kong, S.-C., 2009b. Integration of parallel computation and dynamic mesh refinement for transient spray simulation. Comput. Meth. Appl. Mech. Eng. 198, 1596–1608.

Lippert, A.M., Chang, S., Are, S., Schmidt, D.P., 2005. Mesh Independence and Adaptive Mesh Refinement for Advanced Engine Spray Simulations, SAE Paper 2005-01-0207.

Nomura, Y., Miyagawa, H., Taketoshi, T., Tomoda, T., Kubota, M., Abe, S., 2001. Numerical Study of Mixture Formation and Combustion Process in a Direct Injection Gasoline Engine with Fan Shaped Spray, SAE Paper 2001-01-0738.

O'Rourke, P.J., Amsden, A.A., 1987. The Tab Method for Numerical Calculation of Spray Droplet breakup, SAE Paper 872089.

Patterson, M.A., Reitz, R.D., 1998. Modeling the Effect of Fuel Sprays Characteristics on Diesel Engine Combustion and Emission, SAE Paper 980131.

Pickett, L.M., Siebers, D.L., 2004. Non-Sooting, Low Flame Temperature Mixing-Controlled DI Diesel Combustion, SAE paper 2004-01-1399.

Reitz, R.D., 1987. Modeling atomization process in high pressure vaporizing sprays. Atomization Spray Technol. 3, 309–337.

Rhie, C.M., Chow, W.L., 1983. Numerical study of the turbulent flow past an airfoil with trailing edge separation. AIAA J. 21, 1525–1532.

Sarre, C.K., Kong, S.-C., Reitz, R.D., 1999. Modeling the Effects of Injector Nozzle Geometry on Diesel Sprays, SAE Paper 1999-01-0912.

Schmidt, D.P., Rutland, C.J., 2000. A new collision algorithm. J. Comput. Phys. 164, 62–80.

Siebers, D.L., 1998. Liquid-Phase Fuel Penetration in Diesel Sprays, SAE Paper 980809.

Stiesch, G., 2004. Modeling Engine Spray and Combustion Process. Springer.

Taylor, G.I., 1963. The instability of liquid surfaces when accelerated in a direction perpendicular to their lanes. In: Batchelor, G.K. (Ed.), The Scientific Papers of Sir Geoffrey Ingram Taylor, vol. 3, pp. 532–536.

Torres, D.J., Trujillo, M.F., 2006. KIVA-4: an unstructured ALE code for compressible gas flow with sprays. J. Comput. Phys. 219, 943–975.

Torres, D.J., 2007. Collocated KIVA-4. In: 11th Int. Multidimensional Engine Modelling User's Group Meeting at the SAE Congress, 15 April, Detroit, Michigan.

Tsui, Y., Pan, Y., 2006. A pressure correction method for incompressible flows using un-structured meshes. Numer. Heat Transfer B 49, 43–65.

Von Berg, E., Edelbauer, W., Alajbegovic, A., Tatschl, R., 2003. Coupled Calculation of Cavitating Nozzle Flow, Primary Diesel Fuel Break-Up and Spray Formation with an Eulerian Multi-Fluid Model, ICLASS.

Xue, Q., Kong, S.-C., 2009. Development of adaptive mesh refinement scheme for engine spray simulations. Comput. Fluids 38, 939–949.

Yi, Y., Reitz, R.D., 2003. Modeling the Effect of Primary Atomization on Diesel Engine Emissions, SAE Paper 2003-01-1041.

Yi, J., 2009. Private Communication, Ford Motor Company.